

Metallic nanoparticles irradiated by low-energy protons for radiation therapy: Are there significant physical effects to enhance the dose delivery?

Anne-Catherine Heuskin^{a)}

Namur Research Institute For Life Science (NARILIS), Research center for the Physics of Matter and Radiation (PMR-LARN), University of Namur, B-5000 Namur, Belgium

Bernard Gallez

Biomedical Magnetic Resonance Group (REMA), Louvain Drug Research Institute, Université Catholique de Louvain, B-1200 Woluwé Saint Lambert, Belgium

Olivier Feron

Pole of Pharmacology and Therapeutics (FATH), Institut de Recherche Expérimentale et Clinique (IREC), Université catholique de Louvain, B-1200 Brussels, Belgium

Philippe Martinive

Department of Radiotherapy and Oncology, CHU and University of Liège, B-4000 Liège, Belgium

Carine Michiels

Namur Research Institute For Life Science (NARILIS), Unité de Recherche en Biologie Cellulaire (URBC), University of Namur, B-5000 Namur, Belgium

Stéphane Lucas

Namur Research Institute For Life Science (NARILIS), Research center for the Physics of Matter and Radiation (PMR-LARN), University of Namur, B-5000 Namur, Belgium

(Received 30 November 2016; revised 18 May 2017; accepted for publication 18 May 2017; published 4 July 2017)

Purpose: To identify which physical properties of nanoparticles are correlated with the survival fraction of cells exposed in vitro to low-energy protons in combination with nanoparticles.

Methods: The Geant4 simulation toolkit (version 10.3) was used to model nanoparticles of different sizes (5–50 nm) and materials (Ti, Zr, Hf, Ta, Au, Pt), with or without an organic capping ensuring biocompatibility and to irradiate them with 1.3 or 4 MeV protons and 5.3 MeV alpha particles. The spectra of secondary electrons inside and at the nanoparticle surface were computed, as well as electron yields, Auger and organic capping contribution, trapping in metal bulk and linear energy transfer profiles as a function of distance from the nanoparticle center. In a next step, an in silico cell model was designed and loaded with gold nanoparticles, according to experimental uptake values. Dose to the cell was evaluated macroscopically and microscopically in $100 \times 100 \times 100 \text{ nm}^3$ voxels for different radiation qualities.

Results: The cell geometry showed that radiation enhancement is negligible for the gold concentration used and for any radiation quality. However, when the single nanoparticle geometry is considered, we observed a local LET in its vicinity considerably higher than for the water equivalent case (up to 5 keV/ μm at the titanium nanoparticle surface compared to 2.5 keV/ μm in the water case). The yield of secondary electrons per primary interaction with 1.3 MeV protons was found to be most favorable for titanium (1.54), platinum (1.44), and gold (1.32), although results for higher Z metals are probably underestimated due to the incomplete simulation of de-excitation cascade in outer shells. It was also found that the organic capping contributed mostly to the production of low-energy electrons, adding a spike of dose near the nanoparticle surface. Indeed, the yield for the coated gold nanoparticle increased to 1.53 when exposed to 1.3 MeV protons. Although most electrons are retained inside larger nanoparticles (50 nm), it was shown that their yield is comparable to smaller sizes and that the linear energy transfer profile is better. From a combination of ballistic and nanoparticle size factors, it was concluded that 10-nm gold nanoparticles were better inducers of additional cell killing than 5-nm gold nanoparticles, matching our previous in vitro study.

Conclusions: Although effects from a physical standpoint are limited, the high linear energy transfer profile at the nanoparticle surface generates detrimental events in the cell, in particular ROS-induced damage and local heating. © 2017 American Association of Physicists in Medicine [https://doi.org/10.1002/mp.12362]

Key words: Geant4, gold nanoparticles, low-energy protons, Monte Carlo, protontherapy

1. INTRODUCTION

The interest for radiosensitizers used in combination with radiation therapy is growing and new modalities for cancer treatment are slowly emerging. In particular, the use of nanoparticles (NP) has drawn attention in the recent years. When internalized into tumors, these nanoparticles permitted a higher efficiency of cell killing after irradiation in a number of *in vitro* and *in vivo* studies.^{1–3} In a clinical context, this provides the appealing possibility to reduce the dose delivered to patients and thus radiation toxicity to healthy tissues while maintaining anticancer efficacy.

Until now, most of the work has been focused on sparsely ionizing radiation (X- and γ - rays) and gold nanoparticles. A recent study using HeLa cells assessed the size-dependent radiosensitization of PEG-coated Au-NPs when using gamma rays.⁴ It was found that 12.1 and 27.3 nm Au-NPs provoked the highest radiation enhancement effect and were more homogeneously distributed in the cells compared to smaller and larger NPs. A key challenge is the unraveling of the mechanism of action of these nanoparticles in the enhancement of cell killing. The photoelectric effect is the dominant interaction between photons and high Z elements up to 500 keV because it is proportional to $(\frac{Z}{E})^3$. Mass attenuation coefficients for metal and water differ largely when the photon energy is just above the K edge of high Z elements. The result of this process is the production of secondary electrons, then de-excitation with characteristic x ray and Auger electron emission, giving rise to additional dose to the cell.⁵ However, macroscopic assessment of this extra dose is usually not sufficient to justify the increase in cell killing and studies about local energy deposition patterns at the nanoscale are necessary. Due to limitations in most Monte Carlo methods, the bridge between the macroscopic and the microscopic stages is difficult to establish. Usually, the phase space from the macroscopic simulation is used as an input for the microscale stage. However, a number of parameters in the micro-geometry directly impact the computed dose enhancement ratio (DER). In a recent Monte Carlo study, Zygmanski *et al.* evidenced configurations that artificially increase DER.⁶ In particular, the micro-beam size, the source-to-sample distance or angular properties of primary particles can be a source of bias. In a microscale study, Carter *et al.* showed that incoming x rays were locally absorbed by the nanostructures which in turn released low-energy electrons, giving rise to a high local concentration of free radicals.⁷ A number of simulation studies successfully correlated the nanoscale dose deposition around Au-NPs to cell survival.^{8,9} However, the effect is more important when using kV photons and remains limited in the MV range. In an experimental study assessing the effect of gold nanoparticle sizes, Chithrani *et al.* exposed HeLa cells to photons of different energies (105 and 220 kVp, a clinical 6 MV beam and 660 keV radiation emitted by ¹³⁷Cs).¹⁰ The radiation sensitization enhancement factor was shown to decrease consistently with increasing photon energy. The same finding was evidenced in a Monte Carlo study where kV photons impinging on gold

nanoparticles were shown to produce secondary electrons with the longest range in water compared to MV photons.¹¹ At a distance of 1 μm from the Au-NP surface, this led to a dose two times higher for 150 kVp photons.

Interactions between nanoparticles and radiation are quite different when charged particles, such as protons, are used. Secondary electrons produced by ionization of the atoms contained in the nanostructures have a much shorter range than in the x-ray situation. It is therefore generally assumed that the NPs located outside the cell would not contribute to cell killing. Moreover, the number of protons necessary to achieve a given dose is very low given their high ionization density in the Bragg peak, which thus limits interactions between the beam and nanoparticles. Monte Carlo studies using a proton point source suggest that microscopic dose enhancement is achievable but more realistic source configurations show that physical effects play a minor role in the amplification of damage.^{12–14} In an attempt to identify relevant physical effects at play for protons, Cho *et al.* irradiated vials of gold nanorods in the spread-out Bragg peak (SOBP) region and assessed the contribution of particle-induced x-ray emission (PIXE), particle-induced gamma ray emission (PIGE), Auger electrons, secondary electrons, and activation products.¹⁵ They concluded that only Auger and secondary electrons significantly contribute to dose enhancement but only at short distances (< 100 nm). In a TOPAS study, Lin *et al.* assessed vasculature damage induced by gold nanoparticles homogeneously distributed in blood vessels or confined at vessel walls.¹⁶ They concluded that the extra dose provided by Au-NPs irradiated by a clinical proton beam was about 0.2% and 2% in the homogeneous and wall-confined situations, respectively. Despite an average increase that was not large, they evidenced dose spikes that elevate the local dose to small parts of the blood vessel at about 15 Gy for a 2-Gy prescribed dose. This feature is even more pronounced for a 30-Gy prescribed dose, suggesting a potential use in hypofractionated treatments. Another Monte Carlo study attempted to elucidate the proton energy dependence of dose enhancement by gold nanoparticles.¹⁷ Two pristine beams of 100 or 195 MeV were incident on simulated water cube. For both cases, the resulting proton energy distribution was computed at several depths. These distributions were then used to irradiate a 20 nm Au-NP. The dose enhancement effect (DEF) was spread to several tens of nanometers both in the radial and depth directions. It was shown that DEF was the highest for incident 100 MeV protons and increased depths in the phantom. Ahmad *et al.* validated a model of proton Bragg peak shift due to the presence of metallic nanoparticles.¹⁸ They observed a material-dependent shift of several millimeters and a narrowing of the Bragg peak in a water phantom both *in silico* and experimentally. Using gafchromic film, a dose enhancement up to 21% was observed at 226 MeV, although the simulated value reached only 5%. The discrepancy between simulated and experimental values was attributed to differences in set-ups and the need for advancements in Monte Carlo physics lists. Overall, they concluded that the change in the Bragg peak distribution must be

accounted for in treatment planning to ensure full tumor coverage.

In vitro experiments with protons are less numerous and showed contradictory results. For instance, Polf *et al.* irradiated prostate carcinoma cells with a clinical proton beam after internalization of 44 nm Au-NPs and obtained 15% enhancement in the relative biological effectiveness.¹⁹ Jeynes *et al.* used a low-energy proton beam to irradiate bladder carcinoma cells loaded with 50 nm Au-NPs, but no enhancement of cell killing was observed.²⁰ In contrast, our recent study using lung cancer cells showed sensitization when 25 keV/ μm protons were used, but not with 10 keV/ μm protons in combination with 10 nm Au-NPs.²¹ Additionally, exposure to heavier ions seems to provide a marked sensitization effect. Work with 70 keV/ μm carbon ions was performed by the group of Liu *et al.*: HeLa cells were irradiated in the presence of 15 nm citrate-capped Au-NPs.²² A remarkable increase in hydroxyl radical production was observed (5.5 fold), as well as a 24.5% increase in RBE. The radiosensitization thus depends on numerous factors: cell line, nanoparticle type and size, concentration, intracellular localization, or energy and nature of incoming radiation. Moreover, investigators are limited by the intrinsic cytotoxicity often observed for nanoparticles of small sizes.

With the aim to identify if physical properties are correlated with the survival fraction of cells exposed to low-energy protons in combination with nanoparticles, we performed Monte Carlo simulations. The latest version of the Geant4 toolkit (10.3) which benefits from a revised atomic de-excitation framework was used to perform all calculations.^{23–25} We mainly focused on secondary electron production and Auger de-excitation. First, a number of material and nanoparticle sizes were swept for secondary electron energy spectra, electron production yields, and linear energy transfer (LET) profile around the NP. In a next step, we closely modeled our previous *in vitro* experiments by adding an organic capping on top of Au-NPs.²¹ To our best knowledge, this is the first study assessing the influence of nanoparticle coating on dose enhancement. Next, our cell line geometry was modeled and loaded with Au-NPs to reflect the localization and the uptake observed experimentally. Then simulations of irradiation were performed with low-energy protons (10 and 25 keV/ μm) and doses relevant to radiobiology, matching the configuration used *in vitro*. Identifying the best nanoparticle candidate and proton irradiation conditions will help to permit the transition to clinical use.

2. MATERIALS AND METHODS

2.A. Monte Carlo Simulations

Monte Carlo simulations were performed using the Geant4 Monte Carlo toolkit (version 10.3).^{23,24} The *G4EmLivermorePhysics* list was used with de-excitation enabled. To efficiently model the Auger cascade, a number of precautions must be ensured. First, the production cuts and the lowest electron energy were lowered from the usual

250 eV value down to 13.6 eV (ionization potential of hydrogen). Particles, including electrons, were tracked down to 13.6 eV and the step length was set to 1 nm. The cuts were ignored for all de-excitation channels (Auger, fluorescence and PIXE) and the Auger cascade was enabled in the settings of the physics list. The shell ionization cross section model was set to “ECPSSR_FormFactor” for the K, L, and M shells.^{26,27} To assess the contribution of the Auger effect in the dose enhancement, this channel was shut down in some simulations, by disabling both Auger de-excitation and Auger cascade but keeping PIXE and fluorescence activated. Two different particle sources were investigated: 1.3 or 4 MeV protons (LET in water of 25 or 10 keV/ μm , respectively). These energies correspond to values reached in the Spread Out Bragg Peak (SOBP) region in a clinical context and thus were used in our previous *in vitro* studies to mimic radiotherapy conditions.²¹ 5.3 MeV α particles (100 keV/ μm) were also simulated to assess the effect of high-LET particles in some cases.

2.B. Simulations with nanoparticle geometry

The first part of the study focused on the irradiation of a single 5 nm nanoparticle (NP) in water medium. Different materials were tested: ⁷⁹Au, ⁷⁸Pt, ⁷³Ta, ⁷²Hf, ⁴⁰Zr, and ²²Ti. A water nanoparticle (WNP) of the same size was also simulated for comparison. Irradiation was performed using a uniform circular source placed at 1 nm in front of the NP and with the same diameter. 10⁶ primary particles were simulated and killed upon exiting NP, for saving computation time. All secondary electrons created inside the nanoparticle were scored for energy (labeled “in” in the following paragraphs). This scoring included all electrons regardless of their origin: electrons ejected from Au outer shells by ionization processes, either by a proton or a secondary electron, and Auger electrons resulting from the de-excitation cascade. Increment in the scoring was performed each time a new electron track was created in the NP region. In addition, electrons crossing the boundary between the Au-NP and surrounding water were considered as reaching the NP surface and labeled “out” for scoring purpose. The “out” electrons were assessed at each step.

Yields of secondary electrons were calculated as the ratio of the number of electrons escaping the metal-NP over the number of electrons escaping a WNP and listed with matching mean electron energy and self-absorption coefficient (proportion of electrons trapped in the metal bulk). Auger de-excitation and cascade were also turned off for Au and Ti-NP to assess the contribution of Auger electrons to the total number of secondaries.

The linear energy transfer (LET) as a function of distance from NP center was computed for each case. The energy deposited radially around the NP was evaluated at each step and distance values were filled in a deposited energy-weighted histogram. Only particles having a creation vertex inside the nanoparticle volume were considered for this energy scoring. This histogram was further normalized by the

number of incoming protons, bin width, and required energy unit. The keV/ μm unit was chosen in order to get straight comparison with the incoming beam.

In a second step, the size effect was investigated for Au and Ti-NPs. Nanoparticles ranging from 5 to 50 nm diameter were irradiated *in silico* and comparisons were made with WNPs of similar sizes. The radial LET was computed for each nanoparticle size and the LET modifying factor (LET-MF) was calculated as the ratio of the radial LET around a NP over the radial LET around the corresponding WNP. In addition, the proportion of electrons lost in the gold bulk was determined and production yields were rescaled per incident proton.

As nanoparticles used in radiation therapy are often surface-treated to ensure biocompatibility, Au-NPs coated with PEG-400 were simulated to detect any change caused by the coating. The geometry is represented in Fig. 1(a). Two configurations were tested: 5 or 10 nm Au core coated with a 2 nm PEG layer. The PEG material was modeled as a $\text{C}_2\text{H}_4\text{O}$ molecule and its density adapted to reflect the usual value found for PEG-400, for example 1.128 g/cm³. The PEG layer was implemented as a shell centered on the Au core, with an inner radius corresponding to the Au core and outer radius equal to the inner radius majored by 2 nm. Contribution of secondaries created in the coating was taken into account in the energy spectrum of electrons created inside the nano object and in the spectrum of electrons reaching NP surface. They were also considered in the radial LET calculation. Electron yields were calculated per incident proton and the contribution of coating in electron number was listed accordingly.

2.C. Simulations with cell geometry

Simulations were also performed for a realistic *in vitro* configuration. An A431 epidermoid carcinoma cell was modeled according to confocal microscopy measurements as an elliptical tube of 3 μm thickness. The semimajor axis was set to 12.2 μm , whereas the semiminor axis was 8.4 μm . Again, according to confocal microscopy data, the cell nucleus was

also modeled as an elliptical tube and embedded in the center of the cell volume (2 μm thick, 8.39 and 5.95 μm for semi-major and semi-minor axes).

According to our previous work using this cell line, the cell uptake for Au-NPs is 0.3 and 0.78 pg/cell for a 5 and 10 nm Au core, respectively.²¹ These figures correspond to $2.37 \cdot 10^5$ and $7.72 \cdot 10^4$ Au-NPs per cell, respectively. Analysis of confocal and TEM microscopy images showed that Au-NPs were mainly present in the cell cytoplasm with some level of aggregation. In this *in silico* study, Au-NPs were scattered randomly in the cytoplasm volume and excluded from the nucleus volume in order to maximize the interactions between gold and the incoming beam. The material chosen for the cytoplasm and nucleus volumes was water. As an alternative model for cell uptake, the cytoplasm material was replaced by water with a small percentage of gold in fraction mass: 0.015 and 0.04% wt for 5 and 10 nm Au-NPs, respectively. The used geometry is represented in Fig. 1(b). Note that the size of nanoparticles was enlarged for illustration purpose.

The cell model was irradiated with 3 Gy protons (1.3 and 4 MeV) or 3 Gy α particles (5.3 MeV). A uniform elliptical source was used and was placed perpendicularly to the cell membrane. Macroscopic dose was computed with and without the gold presence in the whole cell volume. In addition, the dose was scored in voxels of 100 nm side to detect local microscopic changes.

3. RESULTS

3.A. Nanoparticles of different materials

Five nanometer nanoparticles were first irradiated *in silico* with 10^6 1.3 or 4 MeV protons in a water medium. Tested materials ranged from low Z to higher Z and included Ti, Zr, Hf, Ta, Au, and Pt. Figure 2 presents the energy spectra of secondary electrons emitted inside and from Au-NP, Ti-NP, and WNP equivalent. Other materials display similar spectra (data not shown).

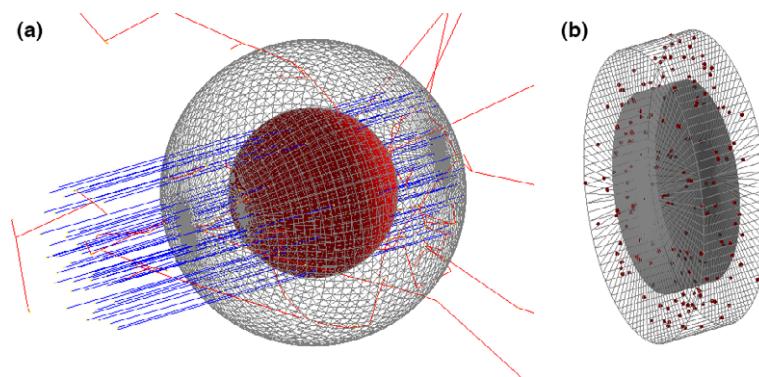


FIG. 1. (a) Simple geometry for single nanoparticle simulations. The gold core is surrounded by a PEG layer. Protons (straight tracks) uniformly irradiate the core. Secondary electrons emerge as nondirectional tracks. (b) Cell geometry: the nucleus is embedded in the cytoplasm. Nanoparticles are scattered through the cytoplasm and are excluded from the nucleus volume. The size of nanoparticles has been enlarged for illustration purpose. [Color figure can be viewed at wileyonlinelibrary.com]

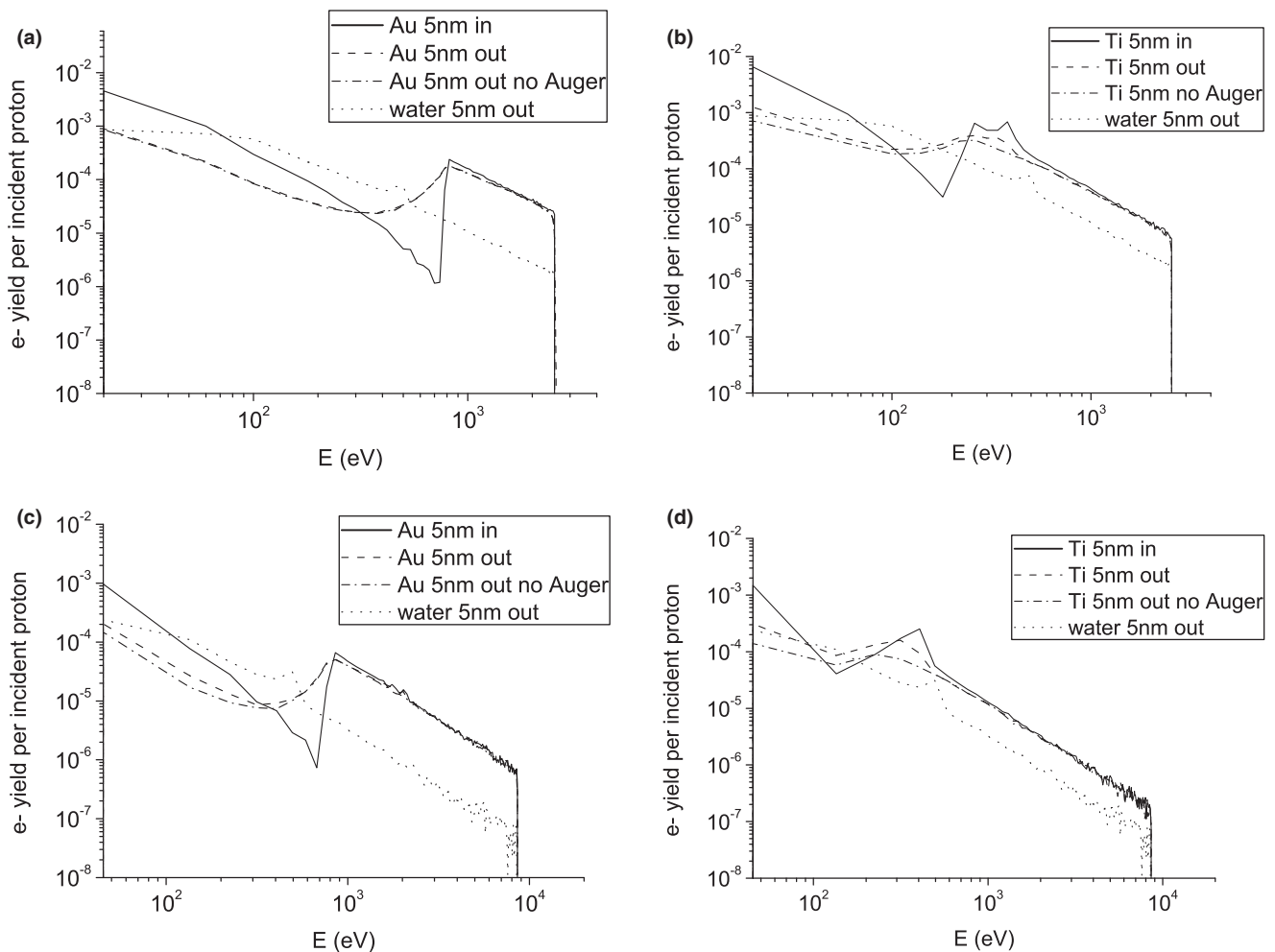


FIG. 2. Energy spectra of secondary electrons emitted from gold or titanium nanoparticles. (a) 5 nm Au-NP irradiated with 1.3 MeV protons (b) 5 nm Ti-NP irradiated with 1.3 MeV protons (c) 5 nm Au-NP irradiated with 4 MeV protons (d) 5 nm Ti-NP irradiated with 4 MeV protons. Plain lines represent the energy spectra inside the nanoparticle whereas dashed lines are for the energy spectra at NP surface. The dash-dotted lines represent the simulations with Auger turned off and the dotted line is for the WNP equivalent. Spectra are normalized per incident proton.

Energy spectra at NP surface are slightly shifted to the left as electrons loose energy to escape the metal. When the Auger process was turned off (dash-dotted lines), the difference was noticeable for Ti-NP at both proton energies and for Au-NP exposed to 4 MeV protons but not to 1.3 MeV protons. An Auger peak for Ti is discernible around 418 eV and corresponds to a LMM transition. Auger from oxygen is also well reproduced for the WNP case at 503 eV (KLL transition). In both cases, 4 MeV protons delivered more energetic electrons. For low projectile energies as those used here, the maximum energy transferred to an atomic electron in a head-on collision can be approximated by the following formula:

$$E_{max} = 2m_0c^2 \left(\frac{\beta^2}{1 - \beta^2} \right).$$

where m_0c^2 is the rest mass energy of an electron and β the velocity of the projectile.²⁸ For 1.3 and 4 MeV protons, this translates to a maximum electron energy of 3.7 and 8.8 keV, respectively.

Table I summarizes the main results for all materials of interest. The yield of secondary electrons is given in comparison to WNP for each case, as well as the mean electron energy for secondaries escaping the NP and the self-absorption coefficient.

Overall, yields followed the same trend as stopping power values for the different materials and more electrons were created in high Z materials. Mean energies were also higher with higher Z and higher proton energy. At the exception of Zr and Ti-NP, electrons originating from metals were on average four to five times more energetic than when arising from the water equivalent. The Auger effect was pronounced for Ti-NP only, with a yield enhancement attributed to Auger of 24 and 55% for 1.3 and 4 MeV protons, respectively. A moderate increase in electron yield was observed for Au-NP irradiated with 4 MeV protons when Auger is turned on (12%). Titanium presented the best electron yield if Auger electrons were considered, followed by platinum and gold. The self-absorption coefficient was in the range of 0.35–0.50 and displayed a similar behavior for both proton energies. The value

TABLE I. Yield of secondary electrons and their mean energy at NP surface for 5 nm NP of different materials irradiated with 1.3 or 4 MeV protons.

		Material								
		Pt	Au	Au Auger off	Ta	Hf	Zr	Ti	Ti Auger off	Water
1.3 MeV protons	Yield	1.44	1.32	1.30	1.19	0.97	1.00	1.54	1.24	1.00
	Mean E (keV)	0.91	0.91	0.92	0.95	0.95	0.68	0.40	0.46	0.23
	Self-absorption	0.52	0.49	0.47	0.41	0.35	0.35	0.53	0.44	0.35
4 MeV protons	Yield	1.86	1.69	1.51	1.54	1.28	1.11	1.94	1.25	1.00
	Mean E (keV)	1.42	1.43	1.54	1.44	1.40	1.01	0.51	0.69	0.32
	Self-absorption	0.51	0.47	0.43	0.40	0.35	0.36	0.56	0.42	0.34

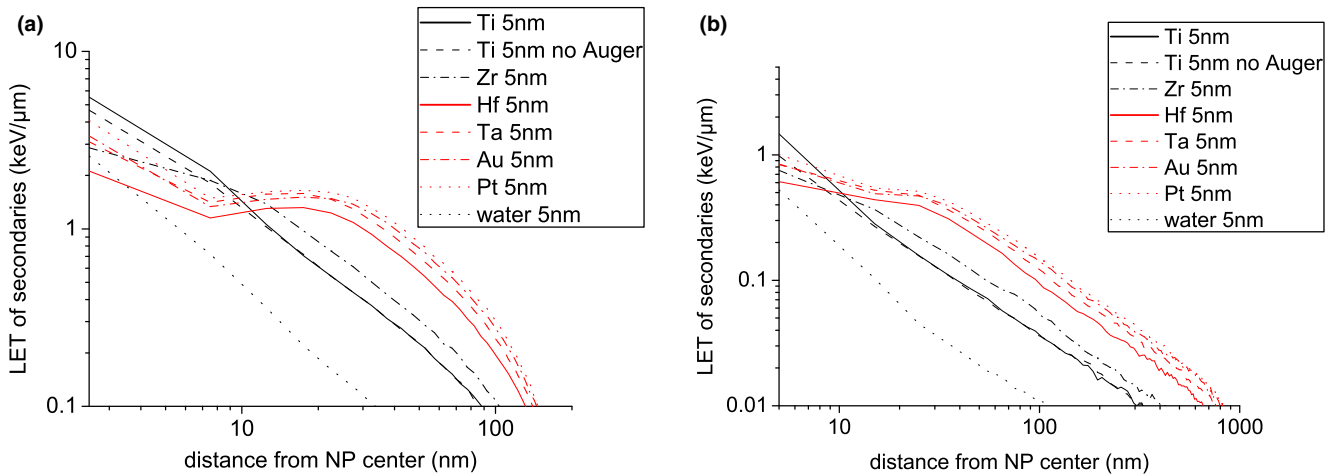


FIG. 3. LET profiles as a function of distance from NP center for different materials. (a) 5 nm NP irradiated with 1.3 MeV protons (b) 5 nm NP irradiated with 4 MeV protons. The black dotted line is for the WNP equivalent. Spectra are normalized per incident proton. [Color figure can be viewed at wileyonlinelibrary.com]

first decreased with decreasing material density down to ≈ 0.35 . Hf-NP absorbed fewer electrons given its lower density and a mean electron energy comparable to heavier metals. For lower atomic numbers (Zr and Ti), the absorption increased despite lower density mainly because the mean electron energy was low. It can also be noted that a lot of Auger electrons were self-absorbed in Ti-NP.

The LET values of secondaries as a function of distance from the NP center are presented in Fig. 3 following NP irradiation with 1.3 or 4 MeV protons.

The effect of metal-NPs spread to about 200 nm and 1 μm from the NP center, whereas the LET from water-originating electrons spread only to 50 nm and 100 nm for 1.3 and 4 MeV protons, respectively. Curves are ordered in the same fashion as stopping power values, except for titanium at short distances where low energy Auger electrons contributed the most to LET, reaching values as high as ~ 5 and 1.4 keV/ μm for 1.3 and 4 MeV protons, respectively.

3.B. Nanoparticles of different sizes

The effect of nanoparticle size on electron yield was investigated for gold and titanium, as candidates for high and low Z, respectively. Sizes were 5, 10, 25, and 50 nm, and NPs

were irradiated *in silico* with 10^6 1.3 or 4 MeV protons. LET-modifying factors (MF) were calculated as the ratio of LET from metal-originating electrons over LET from water-originating electrons as a function of distance from NP center. Results are presented in Fig. 4.

LET-MF decreased with increasing NP sizes in all cases and was higher for Au-NPs. For a given material, values were similar for both proton energies, except at larger distances where more energetic electrons ionized by 4 MeV protons still contributed to LET-MF, giving a steeper slope compared to irradiation with 1.3 MeV protons. The drop at the beginning of curves can be attributed to the small range of low energy electrons. The effect is more pronounced for NP of increasing diameter because the electrons lose a lot of energy to reach the NP surface. Due to Auger electrons, titanium gave a higher LET-MF only in close vicinity to the NP surface and for the smaller diameter (5 nm); at longer distances the lower mean energy of secondaries in comparison to gold yielded lower LET-MF. Electron yields are presented in Table II.

Yields increased with increasing NP diameter after 4 MeV proton irradiation in the gold case only. In the case of 1.3 MeV protons, a slight decrease was observed after 25 nm diameter. Considering the maximum energy of delta electrons issued from 1.3 MeV proton ionization, we hypothesized that

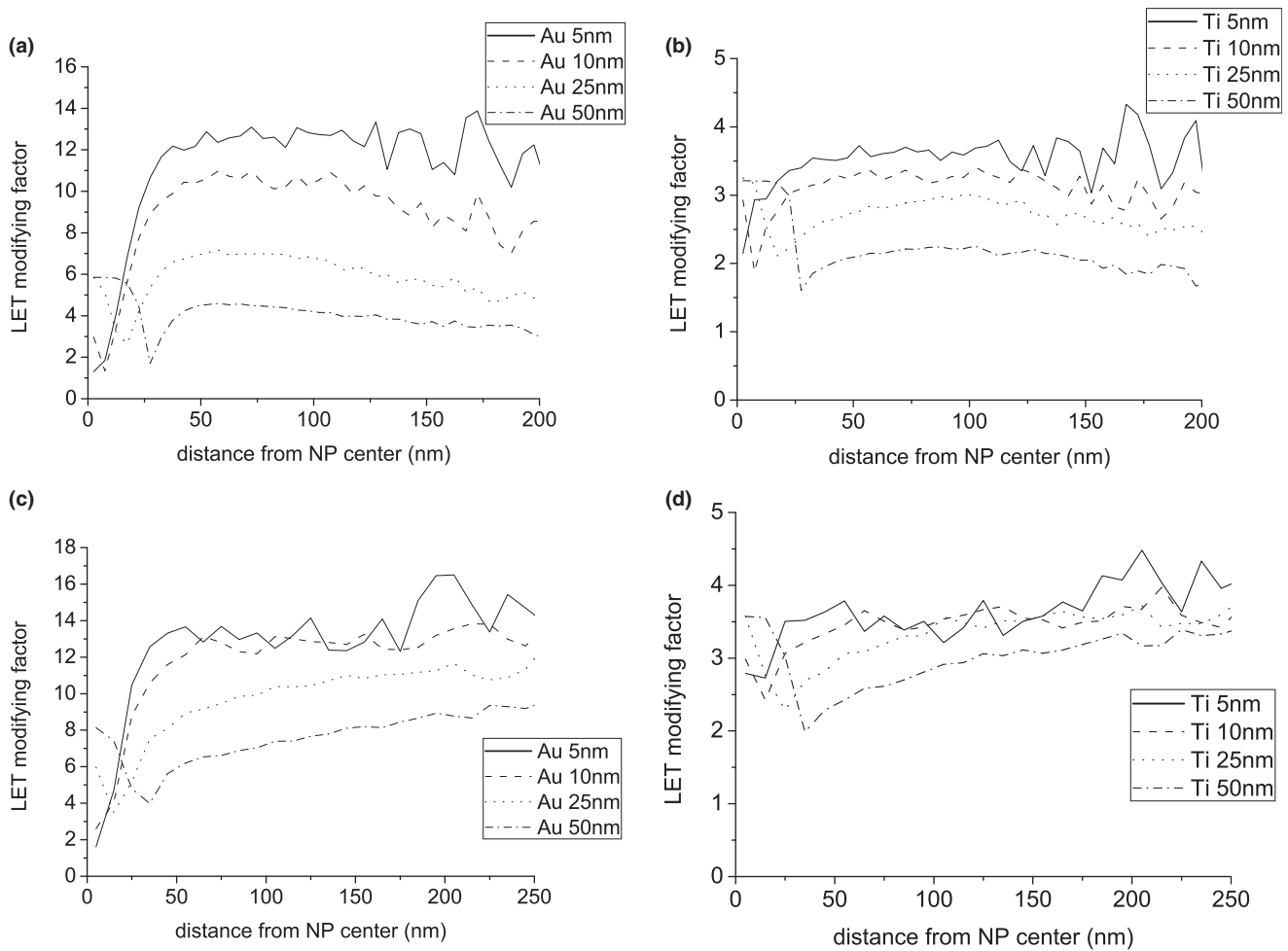


FIG. 4. LET modifying factor as a function of distance from the NP center for Au and Ti-NP of various sizes. (a) Au-NP irradiated with 1.3 MeV protons (b) Ti-NP irradiated with 1.3 MeV protons (c) Au-NP irradiated with 4 MeV protons (d) Ti-NP irradiated with 4 MeV protons.

TABLE II. Yield of secondary electrons at NP surface for gold and titanium irradiated with 1.3 or 4 MeV protons for different NP sizes. Yields are calculated with respect to the WNP of equal diameter.

	Gold				Titanium			
	5 nm	10 nm	25 nm	50 nm	5 nm	10 nm	25 nm	50 nm
1.3 MeV protons	1.32	1.71	1.99	1.89	1.54	1.57	1.56	1.48
4 MeV protons	1.69	2.11	2.61	2.75	1.94	1.88	1.82	1.78

secondary electrons had sufficient energy to travel up to 25 nm in the gold bulk and started to be trapped for larger distances. In contrast, yields for Ti-NP remained constant or slightly decreased with size, due to the lower mean energy of secondaries.

So far, the yields of secondary electrons were calculated with respect to WNP of the same size. However, results differ if we consider the number of secondary electrons produced per incident proton (Table III). The mean electron energy and the proportion of electrons lost in the gold bulk were also assessed for the various sizes and proton energies.

Calculated in this way, the number of emitted electrons kept increasing with increasing NP diameter, although the

effect was less pronounced for Ti-NPs. For both materials, the secondary electrons were more numerous when irradiation was performed with 1.3 MeV protons, as expected as this energy is located in the Bragg peak.

The trapped proportions were similar for both proton energies and both materials, reaching about 96% for 50 nm diameter. However, the yield at 50 nm was higher than for lower NP sizes. This means that the number of secondary electrons created in larger NPs attains a very high amount and that a sufficient proportion is able to reach the NP surface, maintaining a high yield. This correlates with the observation that the mean electron energy increased as the NP diameter increased, originating from a natural filtering of a high

TABLE III. Yield of secondary electrons per incident proton at the surface of gold and titanium NP of different sizes, with corresponding mean electron energy and self-absorption coefficient.

		Gold				Titanium			
		5 nm	10 nm	25 nm	50 nm	5 nm	10 nm	25 nm	50 nm
1.3 MeV protons	Yield	0.20	0.39	0.65	0.76	0.24	0.36	0.51	0.60
	Mean E (keV)	0.91	0.82	0.74	0.72	0.40	0.43	0.49	0.53
	Self-absorption	0.49	0.72	0.91	0.96	0.53	0.74	0.89	0.94
4 MeV protons	Yield	0.08	0.16	0.28	0.38	0.09	0.14	0.20	0.24
	Mean E (keV)	1.43	1.39	1.48	1.64	0.51	0.58	0.79	0.99
	Self-absorption	0.47	0.70	0.89	0.95	0.56	0.75	0.89	0.94

number low-energy electrons. This did not hold for Au-NP exposed to 1.3 MeV protons, where the mean electron energy decreased with NP size. This can be explained by the combination of both higher material density and the lower amount of energy transferred by protons to ionized electrons.

3.C. Coated nanoparticles

The PEG-coated Au-nanoparticles were investigated next. On the basis of our previous *in vitro* studies, cores of 5 or 10 nm Au coated with a layer of 2 nm PEG were simulated and irradiated with 10^6 1.3 or 4 MeV protons, and 5.3 MeV alpha particles. Energy spectra of secondary electrons are presented in Fig. 5 for the 5 nm PEG-coated Au-NP irradiated with 1.3 MeV protons. Other configurations present similar characteristics (data not shown).

Data for the Au-core only are provided for comparison. The WNP equivalent was also computed and its size adapted to reflect the PEG-complex size (9 nm). It can be seen that the PEG coating provides a lot of low-energy electrons that have a spectrum comparable to water-originating electrons. Characteristic Auger peaks are visible for the PEG layer: carbon at 272 eV and oxygen at 503 eV (KLL transitions). The LET of secondary electrons as a function of distance from the NP center is presented in Fig. 6(a). The contribution from

the coating is noticeable at very short distances from NP center (< 25 nm) and results from the low range of the additional low-energy electrons. As a consequence, at NP surface, the LET was doubled compared to the Au core only.

Figure 6(b) displays the LET of secondary electrons for all tested configurations. As for Fig. 3, curves are ordered in the same way as stopping power values. In the case of alpha particles, LET reached values as high as $45 \text{ keV}/\mu\text{m}$ at NP surface for the larger core size.

The yields of secondary electrons are very similar to the values obtained when using Au-NP without coating (Table IV), but are constituted of electrons with slightly less energy on average due to the PEG layer. The PEG contribution can be very high for nanoparticles of smaller sizes (around 40%) as it represented five times more volume than the core itself, but that effect was counterbalanced by the lower ionization rate in PEG compared to gold. On average, the Auger contribution from the coating was 5–6% of total electron number.

3.D. Cell geometry

In the previous simulations, the number of incoming particles (10^6 protons) was unrealistic but required to obtain statistically relevant data. Usually *in vitro* and *in vivo* studies

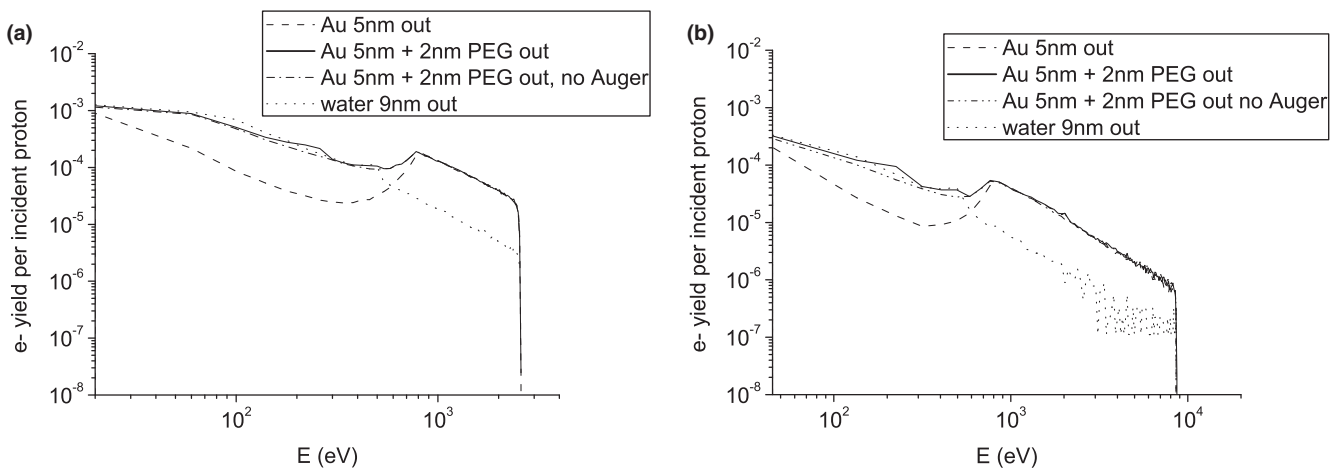


FIG. 5. Energy spectra of secondary electrons emitted from PEG-coated Au-NP. (a) Irradiation with 1.3 MeV protons (b) Irradiation with 4 MeV protons. Plain lines represent the energy spectra at the PEG-complex surface whereas dashed lines are for the energy spectra originating from the Au core only. The dash-dotted lines represent the simulations with Auger turned off and the dotted line is for the WNP equivalent. Spectra are normalized per incident proton.

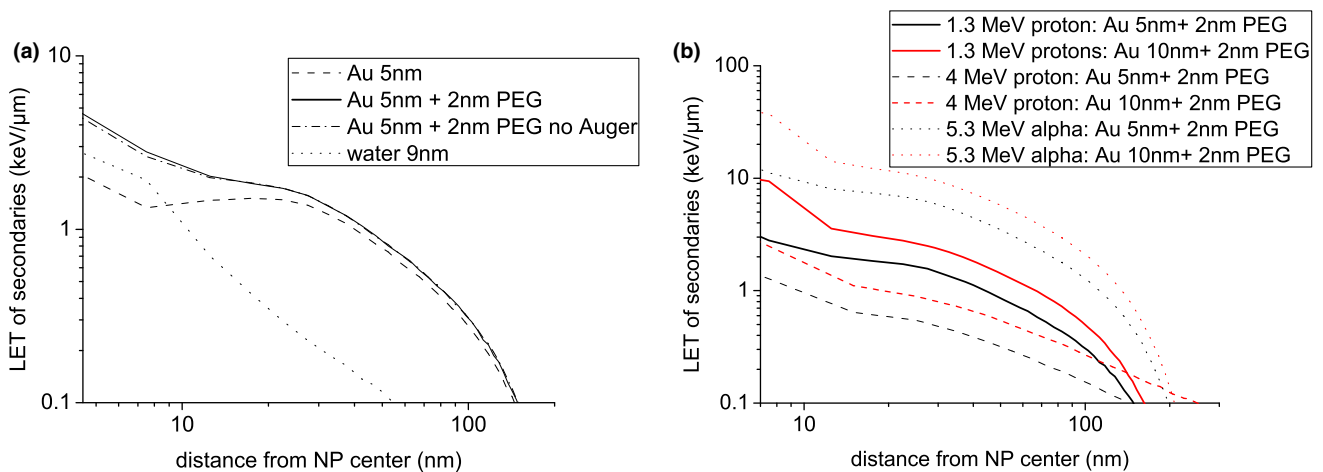


FIG. 6. LET profiles as a function of distance from NP center. (a) PEG-coated Au-NP irradiated with 1.3 MeV protons; the plain line is for the PEG-complex whereas the dashed line is for the Au core only. The dash-dotted line represents simulations with Auger turned off and the dotted line is for the WNP equivalent (b) PEG-coated Au-NP irradiated with 1.3 MeV protons (plain lines), 4 MeV protons (dashed lines) or 5.3 MeV alpha particles (dotted lines). Simulations were performed for two Au core sizes: 5 nm and 10 nm. Spectra are normalized per incident proton. [Color figure can be viewed at wileyonlinelibrary.com]

TABLE IV. Yield of secondary electrons for PEG-coated Au-NP of 5 or 10 nm core diameter irradiated with 1.3 or 4 MeV protons. The proportion of electrons originating from coating is also provided.

		Au core diameter	
		5 nm	10 nm
1.3 MeV protons	Yield	1.53	1.69
	Coating component	0.38	0.14
4 MeV protons	Yield	1.57	1.94
	Coating component	0.32	0.10

focus on doses in the 0–10 Gy range, which corresponds to about four orders of magnitude less in particle number. In the case of a broad beam perpendicular to the sample, the cell is irradiated following poisson statistics and the mean number of particles reaching the cell is proportional to the beam fluence and the cell surface.²⁹ An A431 cell was modeled according to our previous work²¹ and irradiated with a 3 Gy dose of 1.3 or 4 MeV protons or 5.3 MeV alpha particles in a broad beam configuration. In such a case, the number of incoming particles per cell is 247, 639, and 62, respectively. The gold uptake was modeled first by randomly scattering Au-NPs of 5 or 10 nm diameter in the cytoplasm, and second by using a mixture of water and gold as cytoplasm material. Macroscopic doses and doses in voxels ($100 \times 100 \times 100 \text{ nm}^3$) were computed for all configurations. When nanoparticles were modeled as spheres, the macroscopic dose was not different from the control case for all irradiation regimens. However, noticeable changes were observed for proton irradiation when nanoparticles were modeled as a mixture of gold and water, but not for alpha irradiation. The increase in macroscopic dose was in the order of a few cGy but took into account the dose deposited in gold, which was not the case in the first approach. Figure 7 presents the dose distributions in voxels for the different cytoplasm models in an A431 cell irradiated with

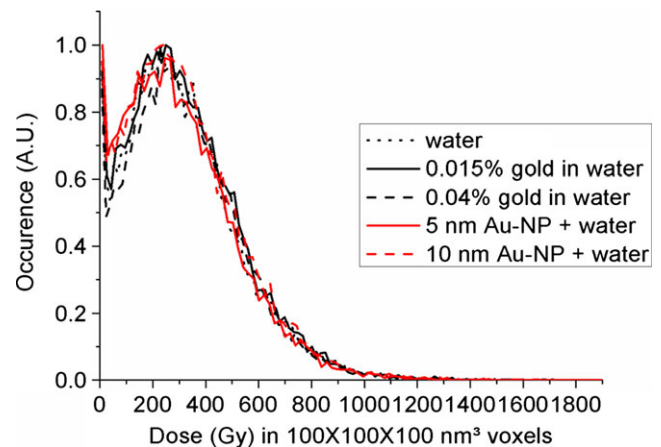


FIG. 7. Dose distribution in $100 \times 100 \times 100 \text{ nm}^3$ voxels in A431 cell model irradiated with 1.3 MeV protons. The cytoplasm content is either water, water with 0.015% gold, water with 0.04% gold water with 5 nm Au-NPs, water with 10 nm Au-NPs. [Color figure can be viewed at wileyonlinelibrary.com]

1.3 MeV protons, excluding voxels with zero dose. Similar results were obtained for 4 MeV protons and 5.3 MeV alpha particles (data not shown). The large peak is attributed to the proton track core (located around 300 Gy), whereas occurrences below 50 Gy results from delta electrons. The signature of Au-NPs was not highlighted in the dose distribution for either case.

4. DISCUSSION

In this work, Monte Carlo simulations using Geant4 were performed in order to identify what type of dose enhancement effect could be obtained for various nano objects differing in term of size and material. The cell geometry showed that radiation enhancement at the macroscopic level is negligible for the metal concentration observed in our previous *in vitro* study. However, when the single nanoparticle

geometry is considered, we observed a local LET in the NP vicinity considerably higher than for the water equivalent volume. This suggests that the dose enhancement effect should be assessed at the nanoscale level.

The yield of secondary electrons for the different metals discussed above is the most favorable for titanium, followed by platinum and gold. While simulations are probably accurate for titanium, this may not be the case for larger Z elements. Indeed, Auger electrons were not evidenced for gold *in silico* at low proton energies (1.3 and 4 MeV). There are two main reasons for this. The first is that cross-sections used in the de-excitation module after proton ionization are only available up to the M shell in this version of Geant4, which means that only de excitations originating from vacancies in the K to M shells could be observable. The second is that the maximum energy transferred by the incoming proton to an electron at rest (3.7 and 8.8 keV for 1.3 and 4 MeV protons, respectively) is not large enough to ionize gold inner shells. The binding energy range for K to M shells is given in Table V in the case of gold and titanium.³⁰ It can be observed that neither 1.3 nor 4 MeV protons could ionize gold further than its M shell. Most ionizations will take place in the outer shells (N and O) and vacancies created there are not followed by the current version of Geant4. Following ionization, two channels of de-excitation are available: emission of a characteristic x ray or emission of an Auger electron. For ionizations taking place in gold outer shells, the latter is the most probable, as its probability increases with increasing shell number (e.g. fluorescence yield = 0.0245 for the M shell in gold in Table V).³¹ It is thus very likely that our simulations underestimated the yield of Auger electrons for high Z targets. These results are in agreement with the work of Incerti et al. where Au-NPs of 10 or 100 nm diameter were irradiated *in silico* with 1 or 10 MeV protons.²⁵ In particular, energy spectra inside and at NP surface were very similar to the data presented here. They concluded that despite the revised atomic de-excitation in Geant4, Auger lines did not produce a significant increase in electron yield after proton irradiation. In contrast to gold, the inner shell of titanium can be ionized by low-energy protons given the lower binding energy. The most probable channel for Ti de-excitation is also Auger, as there is only a small amount of fluorescence from the K shell (Table V). In this case, all K and L vacancies are followed by the code, producing an Auger peak in the emission spectra.

TABLE V. Binding energies and fluorescence yields for the K, L, and M shells in gold and titanium.

		K shell	L shell	M shell
Au	Fluorescence yield	0.9604	0.331	0.0245
	Binding energy (eV)	80725	11919–14353	2206–3425
Ti	Fluorescence yield	0.2256	0.00321	$8.46 \cdot 10^{-6}$
	Binding energy (eV)	4966	453.8–560.9	32.6–58.7

For low-energy protons, it results that the dose enhancement for both gold and titanium nanoparticles comes from a combination of proto-electrons (i.e. resulting from ionizations) and Auger electrons. In the study of Kim et al., the dose enhancement provided by the presence of Au-NP was attributed to PIXE effect.³² Au-NP loaded-cells were irradiated with 45 MeV protons and a drastic effect was observed on cell viability after 20 Gy radiation compared to the proton only scheme. This proton energy is sufficient to ionize the inner K shell of gold atoms, for which the preferential de-excitation channel is x-ray emission. However, the contribution of Auger de-excitation is predominant for all other shells. It follows that fluorescence from gold might only have a minor effect on cell killing.³³

In a clinical protontherapy context, this translates into two main de-excitation schemes according to the Au-NP depth in the patient. The mean proton energy would be very different at the proximal or distal edge of the tumor, the former undergoing an important proportion of high energy protons and the latter mainly Bragg peak protons. Protons reaching the distal edge would only be able to ionize the outer shells of a nanoparticle. The type of interaction between the incoming proton and the nanoparticle and its de-excitation would thus depend on its location in the tumor as illustrated in Fig. 8. At the distal edge where most protons reach the Bragg peak, Au-NPs would release mostly proto-electrons and Auger electrons from outer shells. However, Au-NP-proton interactions at the proximal edge of a tumor would produce proto-electrons and Auger electrons as well as a small amount of larger range characteristic x rays, showering the adjacent tissue.

The size effect of Au and Ti-NPs was also investigated. By comparison to the corresponding WNP, it was found that yields were higher with increasing size in the case of gold and remained constant or were slightly lower for titanium. We attributed this behavior to the difference in average energy of secondary electrons for both materials. In gold, more energetic electrons could reach the NP surface up to 25 nm diameter, whereas it was not the case for titanium. The proportion of trapped electrons was also increasing with NP diameter, reaching about 96% for larger sizes. Similarly, in the work of Cho et al. Au-NPs from 2 to 100 nm diameter were modeled and irradiated *in silico* with SOBP protons.¹⁵ They found out that the energy self-absorbed in NPs was about 1.4% in NPs of smaller sizes and reached 31.1% for 100 nm Au-NPs. This shows that despite a large self-absorption for larger NPs, electrons were filtered to higher energies and about 70% of energy could reach the NP surface.

The LET-modifying factors were also introduced to compare the different NP sizes. The LET-MFs decreased with increasing NP diameter in all configurations and increased with distance from NP center with increasing proton energy. This is in opposition with the increasing number of electrons produced per incident proton with increasing NP size and decreasing proton energy. In general, quantities compared to a water reference yield higher values with increasing proton energy (or decreasing NP size) because the relative difference between stopping powers in water and in metal increases as

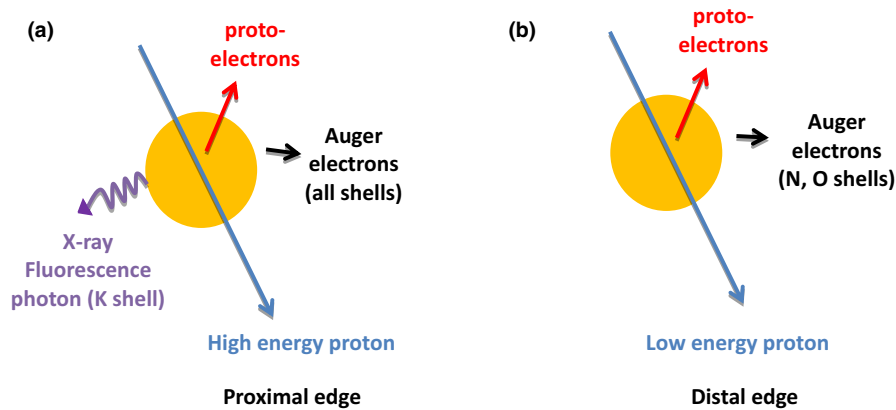


FIG. 8. De-excitation of an Au-NP according to its position in a tumor: (a) proximal or (b) distal edge. [Color figure can be viewed at wileyonlinelibrary.com]

well, whereas quantities computed per incident proton give higher values for decreasing proton energy (or increasing NP size). The same findings were evidenced in the study of Tran *et al.*,³⁴ who assessed the effect of protons from 2 to 170 MeV on a 50 nm Au-NP. The computed dose enhancement factors (DEFs) were best for energetic protons and increased with distance from NP; however, the number of secondary electrons produced was higher when the proton energy decreased. They concluded that there was a competition between DEF and absorbed dose. Therefore, the used reference is crucial for the interpretation of results and has to be well understood. A common confusion is that the metal-NP replaces a hypothetical WNP and the DEF can thus be used. However, metal-NPs are added to the cell volume. In this sense, we feel that it is best to compute results as absolute values per incident proton.

The study of Au-NPs was further carried out by the addition of an organic capping layer: a 2 nm PEG shell was added on top of 5 or 10 nm Au core. The low-energy secondary electrons created in the coating added a water-like component in the energy spectra. This translated into a higher LET very close to NP surface compared to the situation with the Au core only [Fig. 6(a)]. The increased ionization density introduced by NPs leads to dose inhomogeneity locally and triggers the production of a high concentration of reactive oxygen species (ROS) as the production of chemical species is driven by the physical stage. The addition of an organic capping thus adds a local spike in LET and ROS generation very locally. However, the capping should not be too thick if one does not want to lose the advantages of high ionization density in metal. Spaas *et al.* recently demonstrated that there was an average loss of 5.2% in radiosensitivity per nanometer of organic capping.³⁵

In our previous *in vitro* study, it was concluded that 10 nm PEG-Au-NPs combined to 1.3 MeV protons were more efficient in cell killing than when using lower NP diameter or higher energy protons.²¹ This could be explained by the LET profiles shown in Fig. 6(b). The LET of secondary electrons is higher for larger NP diameters and lower proton energies and spreads farther away from NP center. This artificially increases the LET of the proton track, usually correlated with

lower survival fractions. It can be concluded that the LET addition provided by Au-NPs in absolute value per proton is correlated with higher efficiency in cell killing. As shown in Fig. 6(b), *in silico* irradiation of Au-NPs by 5.3 MeV alpha particles led to a very high LET in close vicinity from the NP surface. This could theoretically result in high cell killing efficiency if a sufficient number of interactions occurs between the alpha beam and Au-NPs but this has to be checked experimentally.

The calculations described so far in our work are very different from the situation found in a clinical context or in *in vivo* studies. In particular, the number of protons interacting with a Au-NP is really low at relevant doses. We chose to model a cell geometry to assess how nanoparticles can contribute to dose enhancement in a more realistic context. When evaluated macroscopically or in $100 \times 100 \times 100$ nm³ voxels, the dose increased only when the inclusion of Au-NPs was modeled as a mixture of gold and water with weight proportions respected. This approach was also adopted in several other studies. The addition of 0.03% wt of gold in water lead only to 0.01% of extra energy when gold nanorods were irradiated in the SOBP region in a Geant4 simulation.¹⁵ In another investigation based on the SRIM software, a 10% mixture yielded a 5–6% increase in energy loss ratio between the Bragg peak value and the entrance value in tissue for 100 MeV protons.^{36,37} By comparison, our uniform mixture model yielded between 1.3 and 2% increase in macroscopic dose. The mixture model takes into account the energy deposited in the gold bulk in dose calculation. This energy does not normally participate to the dose deposition as it is not dispersed in the cytoplasm. However, it could be postulated that energy dissipated inside Au-NPs could participate in a thermal effect in the cell. Surdutovich *et al.* used a simple thermodynamic formalism to assess the increase in temperature after the passage of a 0.3 MeV/n carbon ion in a water tube of 10 nm radius.³⁸ They found a 10°C increase, while reducing the tube diameter to 3 nm led to a 100°C increase. Using the same approach for protons, the increase in temperature in a 3 nm water tube was about 13 and 35°C for 4 and 1.3 MeV protons, respectively. If gold was used instead, the increase reached 260 and 140°C, respectively. If a 10 nm tube

was chosen, the increase in temperature in gold still reached remarkable values of 23 and 13°C, respectively. Local heating could be detrimental for the cell if nanoparticles are located close to DNA: it was shown that the melting temperature of DNA is around 85°C but the probability for such an event to occur is rather limited (0.5% for a track at 1 nm from the surface of a nucleosome).³⁹ However, if nanoparticles are located in the cytoplasm, the increase in temperature would be sufficient to alter the integrity of crucial proteins, similarly to what is observed for ROS. Ultimately, this could disrupt organelle function and impair cell viability. Previous studies evidenced changed in cell morphology upon moderate heating (from 38.7 to 42.5°C) and disruption of actin bundle filaments.⁴⁰ In particular, heat-stressed endothelial cells showed increased *Hsp70* mRNA expression, which is mainly involved in partial refolding of damaged proteins, protein disposal and aggregation prevention.⁴¹ Higher temperatures could lead to *Hsp70* exhaustion and accumulation of damaged proteins. Studies on magnetic nanoparticles already showed their high heating capacity upon application of alternating magnetic field.⁴² It is not currently known if irradiation of high-Z metals could lead to the same effect but this is certainly worth investigation. The idea of hyperthermia as an addition to radiotherapy is not new: temperatures between 40 and 44°C were shown to be cytotoxic for cells in a low oxygen or low pH environment, a situation commonly found in tumor cells due to low perfusion.⁴³

Our second approach specifically modeled the Au-NPs as spheres distributed in the cell cytoplasm, but the simulations showed that there was no increase in macroscopic or microscopic dose. It has to be noted that the interaction probability of a Au-NPs with the incident beam is very low, especially when charged particles are considered. Depending on the proton energy, the number of incident particles for a 3 Gy dose is about 250 or 640 for 1.3 and 4 MeV protons, respectively, in our cell model. According to the gold content used here, this translates to a 10^{-6} – 10^{-5} fraction of nanoparticles actually interacting per Gy of radiation, with the lower values for smaller Au-NPs. This is in the same range than the one found in a study of Lin *et al.*⁴⁴ In a TOPAS simulation, a cell model loaded with Au-NPs ranging from 2 to 50 nm was irradiated in the SOBP region. Interestingly, the lower interaction probability per Gy of radiation was found for the smaller nanoparticles, but they were also the most efficient to induce cell killing for the same gold weight. They concluded that the better efficiency of 2 nm Au-NPs was due to their lower internal absorption of secondary electrons and their higher number. The same findings were highlighted in the work of Chithrani *et al.* where the decreased survival fractions assessed by clonogenic assays were correlated with the number of nanoparticles internalized in HeLa cells, rather than gold mass.¹⁰ 14, 50, and 74 nm Au-NPs were used as radiosensitizers in addition to 220 kVp x rays. Despite the higher gold mass internalized for 74 nm Au-NPs, they were present in a lower number than 50 nm Au-NPs which were more efficient. As the

internalization is not controlled, we chose to use previous experimental gold mass values for 5 and 10 nm Au-NPs in A431 cells.²¹ Both in experimental and *in silico* conditions, the 10 nm Au-NPs seemed to be more efficient in cell killing and dose enhancement, respectively. As the cell uptake for 5 and 10 nm Au-NPs does not correspond in gold mass (0.3 and 0.78 pg/cell, respectively) or in nanoparticle number ($2.31 \cdot 10^5$ and $7.72 \cdot 10^4$, respectively), the explanation for the superior effect of 10 nm Au-NPs is more complex. The important quantity to consider from a ballistic standpoint would be the total area of NPs exposed to the beam on the basis of gold mass and nanoparticle size. In our case, the total section exposed is about 4 and 6 μm^2 for 5 and 10 nm Au-NPs, respectively. On one hand, 10 nm Au-NPs have a higher section exposed, and on the other hand a better LET profile for a given proton energy, leading to a superior efficacy. Despite the very high LET induced by alpha particle irradiation on Au-NPs, no dose enhancement was observed. This can be attributed to the even lower interaction probability in the case of alpha particles: less than one nanoparticle is actually irradiated at a 3 Gy dose.

Geant4 studies from other groups assessed the effect of nanoparticles depending on their location in the cell. In general, an homogeneous distribution is assumed but more complex cases were investigated: nucleus or cytoplasm only, and extracellular locations.¹⁵ Sensitizing enhancement ratios were found insignificant for the cytoplasm configuration on the basis of a LEM approach. However, numerous experimental articles highlight the importance of cytoplasm irradiation in genotoxicity or cytotoxicity.^{45,46} Specifically to nanomedicine area, Usami *et al.* irradiated CHO cells with fast ions after incubation with a platinum compound (Pt-terpyridine chloride), which was found to be located in the cytoplasm by nano secondary ion mass spectroscopy.⁴⁷ The cell death rate was largely enhanced although secondary electrons were not able to reach the cell nucleus and create additional DNA damage. Mitochondria and raft structures in the cell membrane were proposed as lethal targets.⁴⁸

5. CONCLUSIONS

In this work, we investigated the LET profiles created in the vicinity of nanoparticles of various materials (from titanium to gold) and the energy spectra of secondary electrons using the Geant4 toolkit with its revised de-excitation module. The implementation of organic coating was also performed for Au-NPs and introduced a significant increase in the production of very low-energy electrons. The best candidates for dose enhancement seem to be gold and platinum due to the higher LET of secondaries. Larger sizes also produced a higher amount of secondary electrons, further increasing the LET. Titanium displays a high amount of Auger effect and thus presented LET superior to gold or platinum at NP surface. However, de-excitation modeling is limited in the sense that only K, L, and M shells are considered.

It is thus highly probable that sensitizing effects from high Z materials are underestimated. Moreover, it is generally assumed that cross-sections available in the Livermore physics list are not accurate below 250 eV. Alternative approaches could be considered: for instance the TRAX code is able to model de-excitation originating from all shells down to 10 eV, but only takes into account electrons and ions so far.⁴⁹ Geometries such as our Au-NP loaded-cell model are also limited in complexity. In a recent study using TRAX, it was shown that 1 over 10 secondary electrons emitted from a Au-NP were produced by Auger effect with a majority of them below 100 eV, which is in strike contrast with Geant4 studies. The Geant4-DNA very low energy extension could help to refine the LET profiles around nanoparticles as well as energy deposition for very low-energy electrons.⁵⁰ Despite limited de-excitation data, this extension features accurate electron cross-sections down to the eV range for a variety of processes (scattering, excitation, ionization, and molecular attachment). Therefore, there is a need for a complete Monte Carlo code, taking into account all shells and particle types, with accurate cross-sections at low energies and able to model complex structures.

Using a cell model with a realistic gold uptake and irradiation conditions, we showed that the dose enhancement provided by Au-NPs was minimal, even when using a uniform mixture model. However, the efficacy of metallic NPs was evidenced in numerous experimental studies, even when they were shown to be located in the cytoplasm. The traditional theory of nucleus being the main target of irradiation seems to be outdated and events occurring in the cytoplasm are of crucial importance for cell killing.

Further experimental work is ongoing to assess the effect of Ti-NPs and Au-NPs combined with alpha particle irradiation. Although effects from a physical standpoint are limited, their high LET profile at NP surface could participate to other detrimental events in the cell. In particular, ROS-induced damage and local heating generated from metallic NPs are likely to become fields of importance in radiation therapy research. Significant efforts will be required to unravel the mechanisms of action of metallic NPs, optimize their effects and move away from a DNA-centrist dogma. This opens up new perspectives in radiation therapy with protons and heavier ions.

ACKNOWLEDGMENTS

TheraPlus project is supported by the Walloon Region, grant n. 1318075. The authors thank S. Penninckx for his help in the design of illustrations.

CONFLICT OF INTEREST

The authors have no relevant conflicts of interest to disclose.

^{a)} Author to whom correspondence should be addressed. Electronic mail: anne-catherine.heuskin@unamur.be.

REFERENCES

- Hainfeld J, Slatkin D, Smilowitz H. The use of gold nanoparticles to enhance radiotherapy in mice. *Phys Med Biol.* 2004;49:N309.
- Hainfeld JF, Dilmanian FA, Slatkin DN, Smilowitz HM. Radiotherapy enhancement with gold nanoparticles. *J Pharm Pharmacol.* 2008;60:977–985.
- Liu J, Liang Y, Liu T, Li D, Yang X. Anti-EGFR-conjugated hollow gold nanospheres enhance radiocytotoxic targeting of cervical cancer at megavoltage radiation energies. *Nanoscale Res Lett.* 2015;10:218.
- Zhang XD, Wu D, Shen X, et al. Size-dependent radiosensitization of PEG-coated gold nanoparticles for cancer radiation therapy. *Biomaterials.* 2012;33:6408–6419.
- Mesbahi A. A review on gold nanoparticles radiosensitization effect in radiation therapy of cancer. *Rep Pract Oncol Radiother.* 2010;15:176–180.
- Zygmanski P, Liu B, Tsiamas P, et al. Dependence of Monte Carlo microdosimetric computations on the simulation geometry of gold nanoparticles. *Phys Med Biol.* 2013;58:7961–7977.
- Carter JD, Cheng NN, Qu Y, Suarez GD, Guo T. Nanoscale energy deposition by X-ray absorbing nanostructures. *J Phys Chem B.* 2007;111:11622–11625.
- Lechtman E, Mashouf S, Chattopadhyay N, et al. A Monte Carlo-based model of gold nanoparticle radiosensitization accounting for increased radiobiological effectiveness. *Phys Med Biol.* 2013;58:3075–3087.
- McMahon SJ, Hyland WB, Muir MF, et al. Biological consequences of nanoscale energy deposition near irradiated heavy atom nanoparticles. *Sci Rep.* 2011;1:18.
- Chithrani DB, Jelveh S, Jalali F, et al. Gold nanoparticles as radiation sensitizers in cancer therapy. *Radiat Res.* 2010;173:719–728.
- Lin Y, McMahon SJ, Scarpelli M, Paganetti H, Schuemann J. Comparing gold nano-particle enhanced radiotherapy with protons, megavoltage photons and kilovoltage photons: a Monte Carlo simulation. *Phys Med Biol.* 2014;59:7675–7689.
- Kwon J, Sutherland K, Hashimoto T, Date H. Dose distribution of electrons from gold nanoparticles by proton beam irradiation. *IJMPCCRO.* 2015;4:49–53.
- Gao J, Zheng Y. Monte Carlo study of secondary electron production from gold nanoparticle in proton beam irradiation. *Int J Cancer Ther Oncol.* 2014;2:02025.
- Martinez-Rovira I, Prezado Y. Evaluation of the local dose enhancement in the combination of proton therapy and nanoparticles. *Med Phys.* 2015;42:6703.
- Cho J, Gonzalez-Lepera C, Manohar N, Kerr M, Krishnan S, Cho SH. Quantitative investigation of physical factors contributing to gold nanoparticle-mediated proton dose enhancement. *Phys Med Biol.* 2016;61:2562–2581.
- Lin Y, Paganetti H, McMahon SJ, Schuemann J. Gold nanoparticle induced vasculature damage in radiotherapy: comparing protons, megavoltage photons, and kilovoltage photons. *Med Phys.* 2015;42:5890.
- Kwon J, Sutherland K, Hashimoto T, et al. TU-H-CAMPUS-TeP3-03: Dose Enhancement by Gold Nanoparticles Around the Bragg Peak of Proton Beams; *Med Phys.* 2014;43:3787–3788.
- Ahmad R, Royle G, Lourenço A, Schwarz M, Fracchiolla F, Ricketts K. Investigation into the effects of high-Z nano materials in proton therapy. *Phys Med Biol.* 2016;61:4537.
- Polf JC, Bronk LF, Driessen WH, Arap W, Pasqualini R, Gillin M. Enhanced relative biological effectiveness of proton radiotherapy in tumor cells with internalized gold nanoparticles. *Appl Phys Lett.* 2011;98:193702.
- Jeynes JC, Merchant MJ, Spindler A, Wera AC, Kirkby KJ. Investigation of gold nanoparticle radiosensitization mechanisms using a free radical scavenger and protons of different energies. *Phys Med Biol.* 2014;59:6431–6443.
- Li S, Penninckx S, Karmani L, et al. LET-dependent radiosensitization effects of gold nanoparticles for proton irradiation. *Nanotechnology.* 2016;27:455101.
- Liu Y, Liu X, Jin X, et al. The radiation enhancement of 15 nm citrate-capped gold nanoparticles exposed to 70 keV/ μm carbon ions. *J Nanosci Nanotechnol.* 2016;16:2365–2370.

23. Agostinelli S, Allison J, Amako K, et al. Geant4—a simulation toolkit. *Nucl Instr Meth Phys Res A*. 2003;506:250–303.
24. Allison J, Amako K, Apostolakis J, et al. Geant4 developments and applications. *IEEE Trans Nucl Sci*. 2006;53:270–278.
25. Incerti S, Suerfu B, Xu J, et al. Simulation of Auger electron emission from nanometer-size gold targets using the Geant4 Monte Carlo simulation toolkit. *Nucl Instr Meth Phys Res B*. 2016;372:91–101.
26. Taborda A, Chaves PC, Carvalho ML, Reis MA. Polynomial approximation to universal M-shell ionisation cross-sections induced by H⁺ and He²⁺ ions. *X-Ray Spectrom*. 2013;42:177–182.
27. Taborda A, Chaves PC, Reis MA. Polynomial approximation to universal ionisation cross-sections of K and L shells induced by H and He ion beams. *X-Ray Spectrom*. 2011;40:127–134.
28. Attix F. Charged-particle interactions in matter. In: *Introduction to Radiological Physics and Radiation Dosimetry*. Hoboken, NJ: Wiley-VCH; 2004: 160–202.
29. Wéra AC, Riquier H, Heuskin AC, Michiels C, Lucas S. In vitro irradiation station for broad beam radiobiological experiments. *Nucl Instr Meth Phys Res B*. 2011;269:3120–3124.
30. Bearden JA, Burr AF. Reevaluation of X-Ray Atomic Energy Levels. *Rev Mod Phys*. 1967;39:125–142.
31. Hubbell JH, Trehan PN, Singh N, et al. A review, bibliography, and tabulation of K, L, and higher atomic shell x-ray fluorescence yields. *J Phys Chem Ref Data*. 1994;23:339–364.
32. Kim JK, Seo SJ, Kim KH, et al. Therapeutic application of metallic nanoparticles combined with particle-induced x-ray emission effect. *Nanotechnology*. 2010;21:425102.
33. Claude Le S, Katsumi K, Noriko U, Yoshiya F, Erika P, Sandrine L. Comment on ‘Therapeutic application of metallic nanoparticles combined with particle-induced x-ray emission effect. *Nanotechnology*. 2012;23:078001.
34. Tran HN, Karamitros M, Ivanchenko VN, et al. Geant4 Monte Carlo simulation of absorbed dose and radiolysis yields enhancement from a gold nanoparticle under MeV proton irradiation. *Nucl Instr Meth Phys Res B*. 2016;373:126–139.
35. Spaas C, Dok R, Deschaume O, et al. Dependence of gold nanoparticle radiosensitization on functionalizing layer thickness. *Radiat Res*. 2016;185:384–392.
36. Torrisi L. Gold nanoparticles enhancing protontherapy efficiency. *Recent Pat Nanotechnol*. 2015;9:51–60.
37. Ziegler J. *The Stopping and Range of Ions in Matter*. Pergamon Press; 1985.
38. Surdutovich E, Obolensky IO, Scifoni E, et al. Ion-induced electron production in tissue-like media and DNA damage mechanisms. *Eur Phys J*. 2009;51:63–71.
39. Surdutovich E, Solov'yov AV. Multiscale physics of ion-beam cancer therapy. *JPCS*. 2012;373:012001.
40. Opie NL, Greferath U, Vessey KA, et al. Retinal prosthesis safety: alterations in microglia morphology due to thermal damage and retinal implant contactmicroglia changes with thermal damage and implant contact. *Invest Ophthalmol Vis Sci*. 2012;53:7802–7812.
41. Tazawa H, Sato K, Tsutiya A, Tokeshi M, Ohtani-Kaneko R. A microfluidic cell culture system for monitoring of sequential changes in endothelial cells after heat stress. *Thromb Res*. 2015;136:328–334.
42. Kulkarni VM, Bodas D, Dhoble D, Ghormade V, Paknikar K. Radio-frequency triggered heating and drug release using doxorubicin-loaded LSMO nanoparticles for bimodal treatment of breast cancer. *Colloids Surf B Biointerfaces*. 2016;145:878–890.
43. van der Zee J. Heating the patient: a promising approach? *Ann Oncol*. 2002;13:1173–1184.
44. Lin Y, McMahan SJ, Paganetti H, Schuemann J. Biological modeling of gold nanoparticle enhanced radiotherapy for proton therapy. *Phys Med Biol*. 2015;60:4149–4168.
45. Wu LJ, Randers-Pehrson G, Xu A, et al. Targeted cytoplasmic irradiation with alpha particles induces mutations in mammalian cells. *Proc Natl Acad Sci USA*. 1999;96:4959–4964.
46. Prise KM, Schettino G, Folkard M, Held KD. New insights on cell death from radiation exposure. *Lancet Oncol*. 2005;6:520–528.
47. Usami N, Furusawa Y, Kobayashi K, et al. ‘Mammalian cells loaded with platinum-containing molecules are sensitized to fast atomic ions. *Int J Rad Biol*. 2008;84:603–611.
48. Kobayashi K, Usami N, Porcel E, Lacombe S, Le Sech C. Enhancement of radiation effect by heavy elements. *Mutat Res*. 2010;704:123–131.
49. Walzlein C, Scifoni E, Kramer M, Durante M. Simulations of dose enhancement for heavy atom nanoparticles irradiated by protons. *Phys Med Biol*. 2014;59:1441–1458.
50. Bernal MA, Bordage MC, Brown JMC, et al. Track structure modeling in liquid water: a review of the Geant4-DNA very low energy extension of the Geant4 Monte Carlo simulation toolkit. *Phys Med*. 2015;31:861–874.